

PF-LHM: 3D Animatable Avatar Reconstruction from Pose-free Articulated Human Images

Lingteng Qiu^{1*} Peihao Li^{1*} Qi Zuo¹
 Xiaodong Gu¹ Yuan Dong¹ Weihao Yuan¹ Siyu Zhu⁵ Xiaoguang Han^{3,4}
 Guanying Chen^{2†} Zilong Dong^{1†}
¹Tongyi Lab, Alibaba Group ²Sun Yat-sen University
³SSE, CUHKSZ ⁴FNii, CUHKSZ ⁵Fudan University

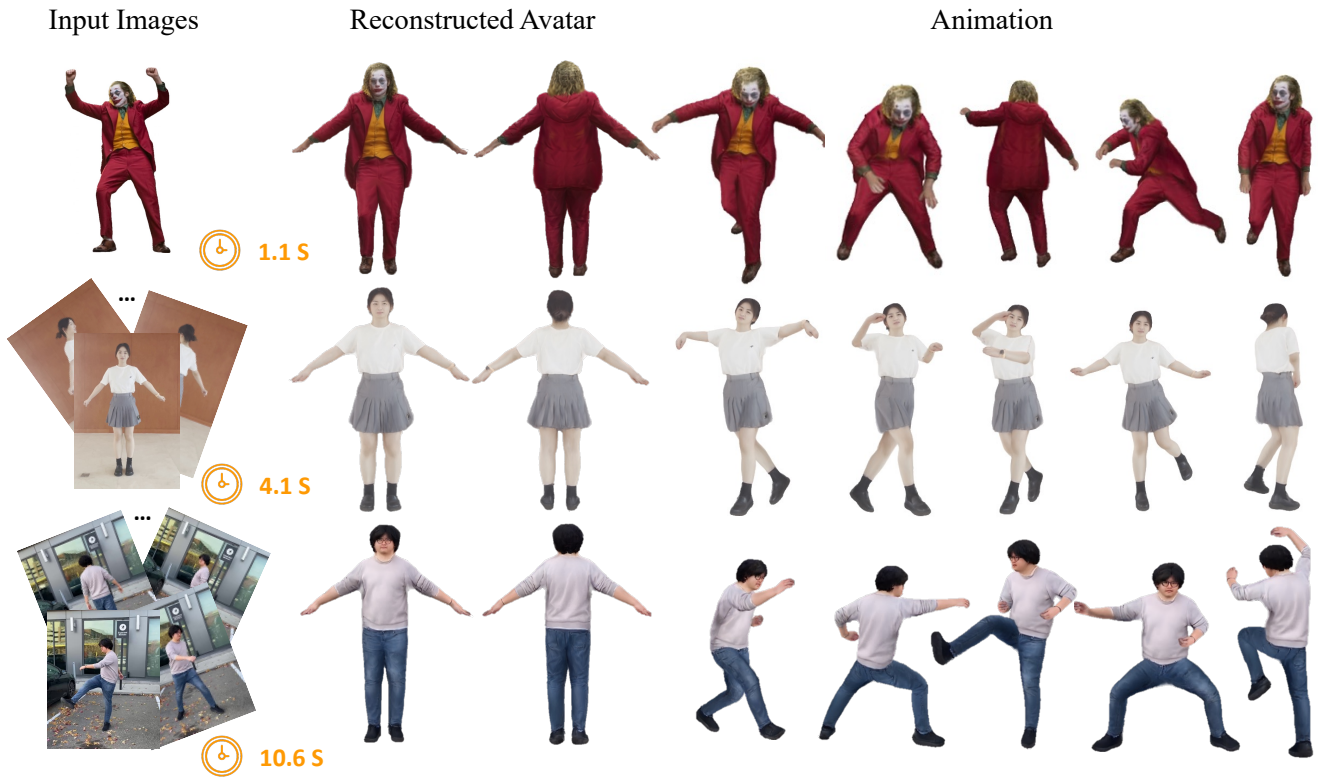


Figure 1. **3D Avatar Reconstruction and Animation Results of our PF-LHM.** Given a set of $N \geq 1$ images of a human subject, without requiring camera parameters or human pose annotations, our method can reconstruct a high-fidelity, animatable 3D human avatar in seconds.

Abstract

Reconstructing an animatable 3D human from casually captured images of an articulated subject without camera or human pose information is a practical yet challenging task due to view misalignment, occlusions, and the absence of structural priors. While optimization-based meth-

ods can produce high-fidelity results from monocular or multi-view videos, they require accurate pose estimation and slow iterative optimization, limiting scalability in unconstrained scenarios. Recent feed-forward approaches enable efficient single-image reconstruction but struggle to effectively leverage multiple input images to reduce ambiguity and improve reconstruction accuracy. To address these challenges, we propose PF-LHM, a large human reconstruction model that generates high-quality 3D avatars

*Equal contribution.

†Corresponding author.

in seconds from one or multiple casually captured pose-free images. Our approach introduces an efficient Encoder-Decoder Point-Image Transformer architecture, which fuses hierarchical geometric point features and multi-view image features through multimodal attention. The fused features are decoded to recover detailed geometry and appearance, represented using 3D Gaussian splats. Extensive experiments on both real and synthetic datasets demonstrate that our method unifies single- and multi-image 3D human reconstruction, achieving high-fidelity and animatable 3D human avatars without requiring camera and human pose annotations. Code and models will be released to the public.

1. Introduction

Reconstructing high-quality, animatable 3D human avatars from casually captured images is a crucial task in computer graphics, with broad applications like virtual reality and telepresence. A practical solution should support rapid and robust reconstruction from minimal input—ideally using only one or a few casually captured images, without relying on camera parameters, human pose annotations, or controlled capture environments. Such capability is essential for enabling scalable and accessible avatar generation in real-world scenarios.

Existing approaches to animatable 3D human reconstruction from monocular or multi-view videos typically rely on optimization-based frameworks that minimize photometric or silhouette reprojection losses [2, 8, 45]. These methods usually require dozens or hundreds of images with accurate human pose estimation as a prerequisite. Moreover, the optimization process is often computationally expensive, taking several minutes or even hours to converge, thus limiting real-time applications.

More recently, LHM [31], a feed-forward network for single-image 3D human reconstruction, has shown promising progress toward real-time performance. It employs a transformer-based architecture to fuse geometric point features initialized from the canonical SMPL-X surfaces and image features to directly predict a 3D Gaussian Splatting [17] based avatar from a single image. However, as single-image-based methods are inherently limited by partial observations, they often struggle to reconstruct occluded or unseen regions, leading to oversmoothed surfaces or noticeable artifacts [34, 60].

A straightforward extension of LHM [31] to multi-image settings would involve concatenating image tokens from multiple images and performing attention fusion. However, such a naive approach suffers from substantial memory and computational overhead due to the large number of geometric point features and the quadratic complexity of dense self-attention mechanisms.

In this work, we propose *PF-LHM*, a novel feed-forward framework for fast and high-fidelity 3D human reconstruction from one or a few images without requiring the camera and human poses. To achieve this, we design an efficient *Encoder-Decoder Point-Image Transformer (PIT) Framework* that hierarchically fuses 3D geometric features with multi-image cues. The framework is built upon *Point-Image Transformer blocks (PIT-blocks)*, which enable interaction between geometric and image tokens via attention fusion while maintaining scalability through spatial hierarchy.

We start by representing the SMPL-X anchor points as geometric tokens and extracting image tokens from each input image. The encoder stage comprises several PIT-blocks to progressively downsample the geometric tokens via Grid Pooling [47]. At each layer, the downsampled point tokens interact with image tokens through multimodal attention [6], allowing compact yet expressive geometric representations to be enriched with visual information from multiple images. The decoder stage upsamples the geometric tokens to recover spatial resolution.

The resulting 3D geometry tokens are decoded to predict Gaussian splatting parameters, enabling photorealistic rendering and animation. To enhance robustness and generalization, we train our model on large-scale real-world human video datasets covering diverse clothing styles, body shapes, and viewing conditions.

In summary, our contributions are:

- We introduce *PF-LHM*, to the best of our knowledge, the first feed-forward model capable of reconstructing high-quality, animatable 3D human avatars in seconds from one or a few casually captured images, without requiring either camera poses or human pose annotations.
- We propose a novel *Encoder-Decoder Point-Image Transformer (PIT)* architecture that hierarchically fuses 3D geometric point features and 2D image features using multimodal attention, enabling efficient and scalable integration of multi-image cues.
- Extensive experiments on both synthetic and real-world data demonstrate that *PF-LHM* unifies single- and multi-image 3D human reconstruction, with superior generalization and visual quality.

2. Related Work

2.1. Human Reconstruction from A Single Image

For single-image 3D human reconstruction, many methods adopt implicit neural representations [4, 33, 34, 49, 50, 53, 57, 59] to model complex human geometries. To improve geometric consistency and generalizability, some approaches [1, 3, 5, 16] rely on parametric body models such as SMPL [21, 26] to predict geometric offsets for the reconstruction of clothed humans. However, reconstruction from a single image is an ill-posed problem. Current

cascade-type approaches [19, 32, 39, 44, 46] attempt to mitigate this issue by decoupling the process into two stages: multi-view image synthesis using generative models, followed by 3D reconstruction. While these methods require view-consistent generation in the first stage, which is often unstable and challenging, this ultimately affects the quality of the reconstruction.

Inspired by the success of large reconstruction models [10, 37], emerging solutions aim to enable direct generalizable reconstruction through feed-forward networks which significantly accelerate the inference time. HumanLRM [46] employs a feed-forward model to decode the triplane NeRF representation, then followed by a conditional diffusion-based novel views generation and reconstruction. IDOL [60] introduces a UV-Alignment transformer model to decode Gaussian attribute maps in a structured 2D UV space. LHM [31] leverages a Body-Head multimodal transformer architecture produces animatable 3D avatars with the face identity preservation and fine detail recovery. While these single-view methods often face challenges with occlusions and invisible regions, frequently resulting in geometrically implausible results or blurred textures, the proposed PF-LHM leverages a variable number of pose-free images to reconstruct photorealistic and animatable avatars.

Concurrent work, GIGA [61], introduces a generalizable human reconstruction model based on UV map representations. However, in contrast to our approach, GIGA requires sparse-view inputs where the same action is captured from multiple viewpoints, along with complex camera setups and motion calibration. These constraints make it challenging to apply in causal scenarios.

2.2. Human Reconstruction from Monocular Videos

Video-based techniques further improve reconstruction consistency by using temporal cues. 4D replay methods [25, 45] can reconstruct dynamic humans from monocular video or multiview video sequences, however, they are not able to drive the humans in novel poses since they do not build a standalone 3D model for humans. Therefore, a series of monocular video-based methods [12, 13, 30, 36] build a static 3D human model and can drive the human in novel poses by binding the skinning weight.

Another series of works [8, 11, 14, 15, 23, 29, 55] take it further by incorporating a 3D parametric human model into the optimization process, and thus can drive the human reconstruction in novel poses without any post-processing. Despite impressive visual fidelity, they often require dozens of minutes and dozens of views for a good optimization, which limits their practical usage in real-world scenarios.

Unconstrained collection is ideal input for a practical application. However, existing methods [51, 54] share a sim-

Table 1. Comparison with state-of-the-art 3D human reconstruction methods. FF stands for Feed-forward, PF for Pose-free, and AM for Animatable.

Method	# Image	FF	PF	AM	Runtime
IDOL [60]	1	✓	✓	✓	Seconds
AniGS [32]	1	✗	✓	✓	15 Minutes
LHM [31]	1	✓	✓	✓	Seconds
Vid2Avatar [7]	> 100	✗	✗	✓	1-2 Days
GPS-Gaussian [58]	2	✓	✗	✗	Seconds
3DGS-Avatar [28]	> 20	✗	✗	✓	0.5 Hours
InstantAvatar [14]	> 20	✗	✗	✓	Minutes
GaussianAvatar [11]	> 20	✗	✗	✓	0.5-6 Hours
ExAvatar [23]	> 20	✗	✗	✓	1.5-5 Hours
PuzzleAvatar [51]	4 ~ 6	✗	✓	✗	4-6 Hours
Vid2Avatar-Pro [8]	> 100	✗	✗	✓	Hours
Ours	≥ 1	✓	✓	✓	Seconds

ilar pipeline that uses a view generative model and score distillation sampling [27] for shape optimization. As a result, they are costly for offline training and impractical for online reconstruction. Paving in a new way, PF-LHM infers a human avatar from one, a few, or dozens of views under any poses in a feed-forward manner and costs only seconds, which is extremely efficient for online applications. Moreover, PF-LHM greatly outperforms any previous state-of-the-art methods on 3D human reconstruction and offers a more flexible input manner for the community.

2.3. Feed-Forward Scene Reconstruction

Recent years have witnessed a paradigm shift in geometric 3D vision, driven by the emergence of methods that eliminate traditional dependencies on camera calibration and multi-stage pipelines. At the forefront of this revolution lies the DUS_t3R [42] framework, which reimagines 3D reconstruction as a direct regression problem from image pairs to 3D pointmaps. By discarding the need for intrinsic camera parameters, extrinsic pose estimation, or even known correspondence relationships, DUS_t3R and its successors [22, 38, 40, 52] have democratized 3D vision, enabling rapid reconstruction across diverse scenarios while achieving state-of-the-art performance in depth estimation, relative pose recovery, and scene understanding. However, general feed-forward reconstruction methods assume that images are captured from a static scene [18, 41], while our PF-LHM can accept multiple human images with different camera and human poses as input and produce an animatable 3D avatar.

3. Method

3.1. Overview

Problem Formulation Given a set of $N \geq 1$ RGB images of a human subject, without known camera parameters or

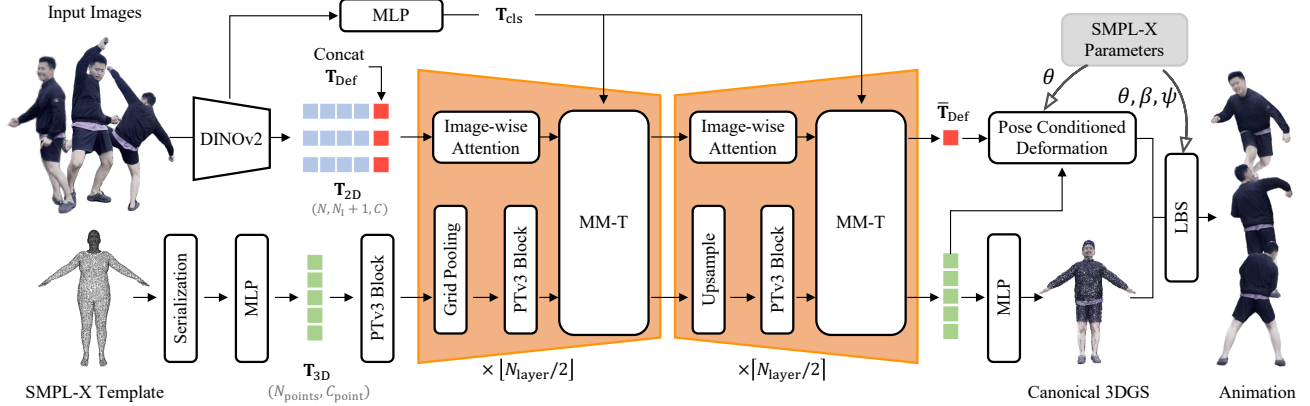


Figure 2. **Overview of the proposed PF-LHM.** In the 2D space, we extract image tokens \mathbf{T}_{img} by DINOv2 from the input RGB images without camera parameters or human poses, which are then concatenated with deformation tokens \mathbf{T}_{Def} to form 2D tokens $\mathbf{T}_{2\text{D}}$. In the 3D space, geometric tokens $\mathbf{T}_{3\text{D}}$ are represented by the MLP output of SMPL-X anchor points. Subsequently, we build our Encoder-Decoder Point-Image Transformer (PIT) to hierarchically fuse 3D tokens with 2D tokens, where the downsampled 3D tokens interact with 2D tokens via multimodal attention in each layer. The finalized 3D tokens are decoded to directly predict 3D Gaussian parameters, enabling animation and photorealistic rendering.

human pose annotations, our goal is to reconstruct a high-fidelity, animatable 3D human avatar in seconds.

We adopt the 3D Gaussians splatting (3DGS) [17] as the representation, which allows for photorealistic, real-time rendering and efficient pose control. Each 3D Gaussian primitive is parameterized by its center location $\mathbf{p} \in \mathbb{R}^3$, directional scales $\boldsymbol{\sigma} \in \mathbb{R}^3$, and orientation (represented as a quaternion) $\mathbf{r} \in \mathbb{R}^4$. In addition, the primitive includes opacity $\rho \in [0, 1]$ and spherical harmonic (SH) coefficients \mathbf{f} to model view-dependent appearance.

Inspired by LHM [31], we employ a set of spatial points $P \in \mathbb{R}^{N_{\text{points}} \times 3}$ uniformly sampled from the SMPL-X surface in its canonical pose to serve as the anchors. Conditioned on the multi-image inputs, these points are processed and decoded to regress the human 3D Gaussian appearance in canonical space through a feed-forward transformer-based architecture. The pipeline can be formulated as:

$$\chi\{\mathbf{p}, \mathbf{r}, \mathbf{f}, \rho, \boldsymbol{\sigma}\} = \text{PF-LHM}(P \mid I^1, \dots, I^N). \quad (1)$$

Model Design A straightforward solution to this problem is to extend LHM to support multiple image inputs by directly concatenating all available image tokens and performing attention operations between 3D point tokens and image tokens. However, this naive extension results in significant computational and memory overhead due to the quadratic complexity of self-attention operations with respect to the total number of tokens, i.e., $\mathcal{O}((N_{\text{points}} + N)^2)$.

To mitigate this issue, we explore strategies to reduce the number of geometric point tokens involved in attention. However, we empirically observe that simply reducing the number of point tokens significantly degrades reconstruction performance. To address this trade-off, we

propose an efficient *Encoder-Decoder Point-Image Transformer Framework* to fuse image features with geometric point features, as illustrated in Fig. 2, which maintains reconstruction quality while reducing the attention footprint.

The final geometric point features output from the decoder are utilized to regress 3D Gaussian parameters using lightweight multi-layer perceptron (MLP) heads. To account for non-rigid deformations such as clothing or hair, we introduce learnable deformation-aware tokens. These tokens, together with the geometric features, are used to predict residual offsets in canonical space. Finally, Linear Blend Skinning (LBS) is applied to animate the canonical avatar into the target pose.

3.2. Encoder-Decoder Point-Image Transformer Framework

To efficiently fuse multi-image features with 3D geometric information, we propose an encoder-decoder architecture based on *Point-Image Transformer blocks (PIT-blocks)*. This framework enables hierarchical feature interaction while alleviating the computational and memory burden associated with dense attention.

We begin by projecting the SMPL-X anchor points in canonical space into a set of geometric tokens and encoding the input images into image tokens, as described in Sec. 3.3. The network consists of N_{layer} PIT blocks, divided into an encoder stage and a decoder stage. In the first $\lfloor N_{\text{layer}}/2 \rfloor$ encoder blocks, we progressively reduce the spatial resolution of the geometric tokens using Grid Pooling [47]. At each layer, the downsampled point tokens perform the attention operation with the image tokens, enabling compact geometric representations enriched with multi-image visual

cues.

In the subsequent $\lceil N_{\text{layer}}/2 \rceil$ decoder blocks, we upsample the geometric tokens to restore their original resolution. At each stage, the upsampled tokens are concatenated with the corresponding high-resolution features from the encoder via skip connections. These fused features are further refined by the PIT blocks to reconstruct detailed geometry and view-dependent appearance.

3.3. Geometric Point and Images Tokenization

Geometric Point Tokenization To incorporate human body priors, we initialize a set of 3D query points $\{\mathbf{x}_i\}_{i=1}^{N_{\text{points}}} \subset \mathbb{R}^3$ by uniformly sampling from the mesh of a canonical SMPL-X pose. Following the design of Point Transformer v3 (PTv3) [48], we first serialize these points into a structured sequence and then project them into a higher-dimensional feature space using an MLP. Formally, this process is expressed as:

$$\begin{aligned} X &= \text{Serialization}(X), \\ \mathbf{T}_{3D} &= \text{MLP}_{\text{proj}}(X) \in \mathbb{R}^{N_{\text{points}} \times C_{\text{point}}}, \end{aligned} \quad (2)$$

where C_{point} denotes the dimensionality of the point tokens.

Multi-Image Tokenization To obtain rich image features, we adopt DINOv2 [24], a vision transformer pretrained on large-scale in-the-wild datasets, as the image encoder \mathcal{E}_{img} . Given an input image I , we extract a sequence of image tokens as follows:

$$\mathbf{T}_{\text{img}} = \mathcal{E}_{\text{img}}(I) \in \mathbb{R}^{N_I \times C}, \quad (3)$$

where N_I is the number of image tokens and C is the output feature dimension of the transformer.

Deformation-aware Token Injection To account for non-rigid deformations such as clothing and hair present in each image, we introduce a learnable deformation token specific to the observed subject, denoted as $\mathbf{T}_{\text{Def}} \in \mathbb{R}^{1 \times C}$. This token is concatenated with the image token sequence \mathbf{T}_{img} , forming the multi-image tokens:

$$\mathbf{T}_I = [\mathbf{T}_{\text{img}}; \mathbf{T}_{\text{Def}}] \in \mathbb{R}^{(N_I+1) \times C}, \quad (4)$$

where $[\cdot; \cdot]$ denotes token-wise concatenation along the sequence dimension.

3.4. Point-Image Transformer Block

After obtaining both geometric and image tokens, we design an efficient *Point-Image Transformer Block* (PIT-block), which comprises three core attention modules to facilitate cross-modal interaction:

Point-wise Attention To model self-attention among geometric tokens, we adopt the patch-based point transformer blocks from PTv3 [48]. This design enables cross-patch

interactions via randomized shuffling of point orders, as detailed in the Supplementary Materials:

$$\mathbf{T}_{3D} = \text{PTv3-Block}(\mathbf{T}_{3D}). \quad (5)$$

Image-wise Attention Given the image token sequence $\mathbf{T}_{2D} = \{\mathbf{T}_1^I, \dots, \mathbf{T}_I^I\} \in \mathbb{R}^{N \times (N_I+1) \times C}$, we apply self-attention independently to the tokens of each image. This updates the features within each frame based on its own image tokens:

$$\mathbf{T}_{2D} = \text{Self-Attention}(\mathbf{T}_{2D}). \quad (6)$$

Point-Image Attention After obtaining the updated features for both point-wise and frame-wise modalities, we develop a global point-image attention mechanism to fuse the point and multi-image tokens. Our model builds upon the powerful Multimodal-Transformer (MM-Transformer) [6] to efficiently merge features from different modalities.

To enhance global context representation in the input images, we utilize the class token \mathbf{T}_{cls} extracted from the first frame as learnable global context features. Additionally, to align the dimensions of different modalities, we incorporate projection MLPs into both the input and output layers of the MM-Transformer (MM-T):

$$\begin{aligned} \bar{\mathbf{T}}_{2D} &= \text{Flatten}(\mathbf{T}_{2D}) \in \mathbb{R}^{N(N_I+1) \times C}, \\ \bar{\mathbf{T}}_{3D} &= \text{MLP}_{\text{proj}}(\mathbf{T}_{3D}) \in \mathbb{R}^{N_{\text{points}} \times C}, \\ \bar{\mathbf{T}}_{3D}, \bar{\mathbf{T}}_{2D} &= \text{MM-T}(\bar{\mathbf{T}}_{3D}, \bar{\mathbf{T}}_{2D} \mid \mathbf{T}_{\text{cls}}), \\ \mathbf{T}_{3D} &= \text{MLP}_{\text{upproj}}(\bar{\mathbf{T}}_{3D}) \in \mathbb{R}^{N_{\text{points}} \times C_{\text{point}}}, \\ \mathbf{T}_{2D} &= \text{UnFlatten}(\bar{\mathbf{T}}_{2D}, N) \in \mathbb{R}^{N \times (N_I+1) \times C}. \end{aligned} \quad (7)$$

This global point-image attention module enables effective fusion of geometric and visual features by leveraging cross-modal attention.

3.5. 3D Human Gaussian Parameter Prediction

Given the fused point tokens \mathbf{T}_{3D} obtained from the encoder-decoder transformer framework, we predict the parameters of 3D Gaussians in the canonical human space using a lightweight MLP head:

$$\begin{aligned} \{\Delta \mathbf{p}_i, \mathbf{r}_i, \mathbf{f}_i, \rho_i, \sigma_i\} &= \text{MLP}_{\text{regress}}(\mathbf{T}_{3D}^{(i)}), \\ \mathbf{p}_i &= \mathbf{x}_i + \Delta \mathbf{p}_i, \quad \forall i \in \{1, \dots, N_{\text{points}}\}, \end{aligned} \quad (8)$$

where $\Delta \mathbf{p}_i \in \mathbb{R}^3$ denotes the predicted residual offset from the corresponding canonical SMPL-X vertex \mathbf{x}_i , and $\mathbf{r}_i, \mathbf{f}_i, \rho_i, \sigma_i$ are the Gaussian orientation, feature vector, opacity, and scale, respectively.

Pose Conditioned Deformation Although the regressed canonical-space Gaussians can be animated to target poses

using Linear Blend Skinning (LBS), modeling clothing deformations presents challenges due to their complex non-rigid motion patterns, which LBS is often unable to capture adequately. To overcome this limitation, we use a lightweight MLP to predict pose-dependent residual deformations.

Specifically, we derive a deformation-aware token $\bar{\mathbf{T}}_{\text{def}}$ by averaging the fused deformation-aware tokens \mathbf{T}_{def} across all frames, and concatenate it with the SMPL parameters to modulate the geometric tokens using Adaptive Layer Normalization. These modulated features are then processed through a sequence of MLP layers to generate non-rigid residual deformations:

$$\Delta \mathbf{p}_i^{\text{motion}} = \text{MLP}_{\text{motion}} \left(\text{AdaLN}(\mathbf{T}_{\text{points}}^{(i)}, [\bar{\mathbf{T}}_{\text{def}}; \boldsymbol{\theta}]) \right), \quad (9)$$

where $\boldsymbol{\theta}$ represents the SMPL pose parameters. The final posed positions are then obtained by adding both canonical offsets and motion-specific deformations before LBS is applied.

3.6. Loss Function

Our training strategy integrates photometric supervision from unconstrained video sequences with geometric regularization on Gaussian primitives. This hybrid optimization framework enables the learning of deformable human avatars without the need for explicit 3D ground-truth annotations.

To better capture complex clothing deformations, we adopt a diffused voxel skinning approach as proposed in [20, 30]. Given the predicted 3DGS parameters $\chi = (\mathbf{p}, \mathbf{r}, \mathbf{f}, \rho, \sigma)$, we transform the canonical avatar into target view space using voxel-based skinning.

Photometric Loss We render the animated Gaussian primitives via differentiable splatting to obtain an RGB image \hat{I} and an alpha mask \hat{M} , based on the target camera parameters. Supervision is applied through the following photometric loss:

$$\mathcal{L}_{\text{photometric}} = \lambda_{\text{rgb}} \mathcal{L}_{\text{color}} + \lambda_{\text{mask}} \mathcal{L}_{\text{mask}} + \lambda_{\text{per}} \mathcal{L}_{\text{lpips}}, \quad (10)$$

where $\mathcal{L}_{\text{color}}$ and $\mathcal{L}_{\text{mask}}$ are L1 losses on RGB and alpha values respectively, and $\mathcal{L}_{\text{lpips}}$ is a perceptual loss measuring high-frequency feature similarity. We set the corresponding weights as $\lambda_{\text{rgb}} = 1.0$, $\lambda_{\text{mask}} = 0.5$, and $\lambda_{\text{per}} = 1.0$.

Gaussian Regularization Loss Empirically, we observe that using only mask supervision tends to encourage overly large Gaussian scales, especially near object boundaries, which leads to blurred renderings. To counteract this issue, we propose a *Mask Distribution Loss* \mathcal{L}_{dis} , which encourages uniform Gaussian distributions within human masks and sharper boundary representation. This is achieved by rendering an auxiliary mask M_{dis} with fixed Gaussian parameters (opacity $\rho = 0.95$, scale $\sigma = 0.002$), and applying a L1 loss between M_{dis} and the ground-truth human mask.

Furthermore, to reduce ambiguities in canonical space supervision, we adopt two additional geometric regularizers from LHM [31]: (1) the *As Spherical As Possible* loss $\mathcal{L}_{\text{ASAP}}$, which promotes isotropy in the 3D Gaussians, and (2) the *As Close As Possible* loss $\mathcal{L}_{\text{ACAP}}$, which preserves spatial coherence among neighboring primitives.

The combined geometric regularization term is defined as:

$$\mathcal{L}_{\text{reg}} = \lambda_{\text{dis}} \mathcal{L}_{\text{dis}} + \lambda_{\text{ASAP}} \mathcal{L}_{\text{ASAP}} + \lambda_{\text{ACAP}} \mathcal{L}_{\text{ACAP}}, \quad (11)$$

with empirically chosen weights: $\lambda_{\text{dis}} = 0.5$, $\lambda_{\text{ASAP}} = 20$, and $\lambda_{\text{ACAP}} = 5$.

Overall Loss The overall training objective combines photometric reconstruction accuracy with geometric regularization:

$$\mathcal{L}_{\text{total}} = \mathcal{L}_{\text{photometric}} + \mathcal{L}_{\text{reg}}. \quad (12)$$

4. Experiments

Implementation Details We design three variants of our model with $N_{\text{layer}} = 4, 6, 8$ layers of the PI-MT block, corresponding to PF-LHM-S (small), PF-LHM-M (medium), and PF-LHM-L (large), respectively. The models contain approximately 500 MB, 700 MB, and 1000 MB training parameters in total. We train the model by minimizing the training loss using the AdamW optimizer for 60,000 iterations. A cosine learning rate scheduler is employed, with a peak learning rate of 0.0001 and a warm-up period of 3,000 iterations. During each batch, we randomly sample a number of frames in the range of [1, 16] from a randomly selected training video. Input images are resized to have a maximum dimension of 1024 pixels. Training is performed on 32 A100 GPUs over five days. To ensure training stability, we apply gradient norm clipping with a threshold of 0.1. Additionally, we utilize bfloat16 precision and gradient checkpointing to enhance GPU memory and computational efficiency.

Training Dataset For our model training, we utilize approximately 300,000 in-the-wild video sequences collected from public video repositories, along with over 5,173 3D public synthetic static human scans sourced from 2K2K [9], Human4DiT [35], and RenderPeople. Specifically, we employ a sampling ratio of 19:1 to draw training batches from the in-the-wild and synthetic datasets to balance generalization and view-consistency. To address view bias in the video data, we sample from a diverse range of perspectives as uniformly as possible, guided by the estimated global orientation of SMPL-X.

Evaluation Protocol We report PSNR, SSIM [43], and LPIPS [56] to assess rendering quality, and measure efficiency with GPU memory usage and inference time.

Table 2. Comparison experiments with sparse-view input methods on public benchmark.

views	InstantAvatar [14]				GaussianAvatar [11]				ExAvatar [23]				PF-LHM-L			
	PSNR	SSIM	LPIPS	Time	PSNR	SSIM	LPIPS	Time	PSNR	SSIM	LPIPS	Time	PSNR	SSIM	LPIPS	Time
2	19.324	0.929	0.136	87 s	13.572	0.863	0.180	90 s	25.534	0.953	0.049	8.5 m	26.544	0.962	0.026	1.65 s
4	20.860	0.928	0.129	143 s	18.201	0.916	0.112	134 s	26.563	0.956	0.043	15 m	26.979	0.962	0.025	2.23 s
8	20.833	0.926	0.134	254 s	21.830	0.942	0.073	216 s	27.573	0.960	0.040	32 m	27.311	0.963	0.023	4.11 s
16	21.075	0.930	0.119	451 s	23.461	0.949	0.059	376 s	28.108	0.962	0.039	1.22 h	27.888	0.965	0.022	10.64 s

Table 3. Comparison experiments with sparse-view input methods on causal videos.

views	InstantAvatar [14]				GaussianAvatar [11]				ExAvatar [23]				PF-LHM-L			
	PSNR	SSIM	LPIPS	Time	PSNR	SSIM	LPIPS	Time	PSNR	SSIM	LPIPS	Time	PSNR	SSIM	LPIPS	Time
2	22.624	0.950	0.079	87 s	18.455	0.935	0.089	90 s	26.723	0.969	0.031	8.5 m	28.229	0.974	0.016	1.65 s
4	23.627	0.954	0.073	143 s	21.073	0.949	0.063	134 s	27.532	0.970	0.028	15 m	28.450	0.974	0.016	2.23 s
8	23.548	0.954	0.071	254 s	23.980	0.960	0.043	216 s	28.431	0.972	0.026	32 m	28.643	0.975	0.015	4.11 s
16	23.420	0.955	0.065	451 s	24.943	0.962	0.037	376 s	28.916	0.973	0.024	1.22 h	28.924	0.977	0.014	10.64 s

4.1. Comparison with Existing Methods

Animatable Human Reconstruction from Sparse Images

We conduct a comprehensive evaluation of PF-LHM by comparing it with three baseline methods for generating animatable human avatars from casually captured video sequences. We assess the efficiency and performance of our model using two types of datasets: one is a public benchmark that includes 20 video sequences from NeuMan [15], REC-MV [30], and Vid2Avatar [7], while the other comprises 24 casual video sequences collected via our smartphones.

Both Table 2 and Table 3 illustrate quantitative experiments evaluating our model against InstantAvatar [14], GaussianAvatar [11], and ExAvatar [23] on public and casual video sequences. Compared to the state-of-the-art (SOTA) baseline ExAvatar, our approach not only significantly accelerates the inference time but also yields comparable quantitative results. Specifically, for the model’s efficiency, our model promptly creates animable avatars in seconds while ExAvatar requires approximately 15 minutes to 1.2 hours, depending on the number of input images. In terms of model performance, SOTA methods typically require dozens of input images to achieve satisfactory metrics; Moreover, our model achieves more accurate results with substantially fewer inputs, and this capability improves as the number of input images increases. As shown in Figure 3, sparse input views lead to noticeable reconstruction artifacts with fitting-based frameworks, including geometric distortions and texture blurring. However, our PF-LHM achieves robust and high-fidelity reconstruction from sparse inputs and outperforms the SOTA baselines.

Animatable Human Reconstruction from a Single Image

We evaluate PF-LHM against three baseline approaches for single-view animatable human reconstruction. The first baseline is AniGS [32], which employs a multi-view diffusion model to create canonical human avatars, followed by 4D Gaussian splatting (4DGS) optimization to

Table 4. Comparison with single-image method on pose animation using our in-the-wild dataset. * indicates we use 80000 query points in LHM for a fair comparison. + denotes the measured inference time of IDOL.

Methods	Input	PSNR \uparrow	SSIM \uparrow	LPIPS \downarrow	Time \downarrow	Memory \downarrow
AniGS [32]	1	17.023	0.858	0.087	15 minutes	24 GB
IDOL [60]	1	17.835	0.871	0.083	1.93 seconds +	23 GB
LHM-0.7B* [31]	1	20.338	0.920	0.047	4.77 seconds	21 GB
PF-LHM-M	1	20.335	0.919	0.047	1.11 seconds	11 GB
	2	20.891	0.923	0.042	1.42 seconds	11 GB
	4	21.172	0.925	0.039	2.02 seconds	13 GB
	8	21.574	0.926	0.037	3.7 seconds	15 GB
	16	21.752	0.928	0.037	9.15 seconds	18 GB

address inconsistencies across different views. The second one is IDOL [60], using a UV-based transformer model to create the animatable avatars training from synthetic human datasets built on a human video diffusion model. The last baseline, LHM [31], introduces novel body-head transformer blocks that directly regress human Gaussian parameters in canonical space. For our evaluation, we employ 400 in-the-wild video sequences featuring individuals of various age groups, including young men and women, older adults, and children. For a fair comparison, we compare LHM with the same parameters and query points. Figure 7 shows a qualitative comparison experiments with LHM on in-the-wild data. The figure indicates that PF-LHM achieves results comparable to LHM with single-view image input. Furthermore, as the number of inputs increases, our method generates increasingly realistic and detailed results.

Table 4 presents two key findings regarding single-view human reconstruction. Our unified framework not only achieves competitive quantitative results compared to LHM but also the inference speed that is four times faster than that of LHM. Furthermore, as the number of input views increases, our method’s performance also improves. Specifically, in comparison to a single-image input, using 16 input views results in improvement of 1.417, 0.09, and 0.01 in PSNR, SSIM, and LPIPS, respectively. Figure 7 shows a qualitative comparison experiment with LHM.

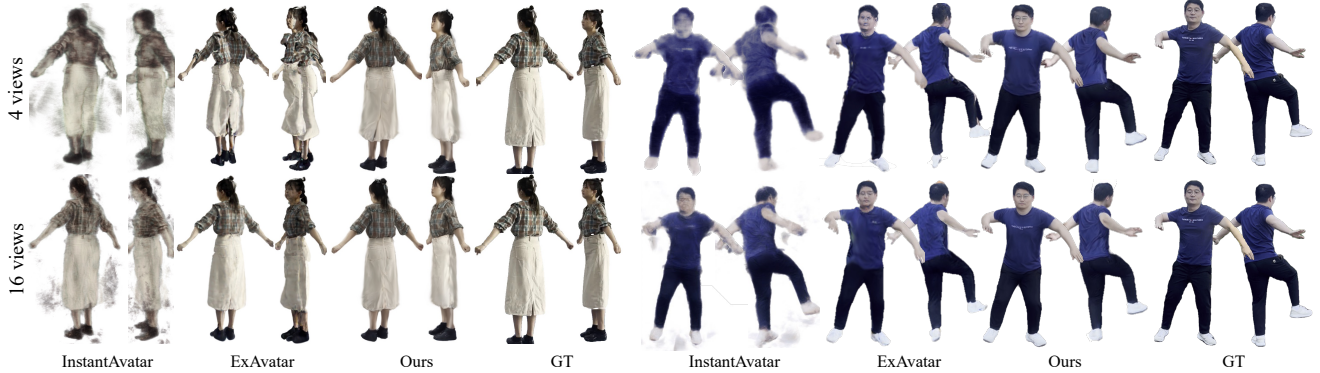


Figure 3. Qualitative results of animatable human reconstruction from sparse-view inputs.

Table 5. **Model Efficiency.** We evaluate the training and inference efficiency of various backbones. The batch size is set to 1, the number of input views is equal to 16. ‘# Points’ refers to the number of geometric points, and ‘Time’ denotes the duration of a single iteration during both training and inference.

Methods	Params.	# Points	Training		Inference	
			Time	Memory	Time	Memory
LHM-0.5 B [31]	500 MB	80 K	26.33 s	54.97 GB	21.61 s	27.8 GB
LHM-0.7 B [31]	700 MB	80 K	50.23 s	62.27 GB	43.06 s	28.3 GB
LHM-1.0 B [31]	1000 MB	80 K	70.61 s	71.55 GB	64.29 s	29.7 GB
LHM-1.0 B [31]	1000 MB	160 K	-	> 80 GB	159.19 s	35.8 GB
PF-LHM-S	500 MB	80 K	8.77 s	46.5 GB	7.35 s	17.0 GB
PF-LHM-M	700 MB	80 K	10.01 s	50.4 GB	9.03 s	18.3 GB
PF-LHM-L	1000 MB	80 K	11.13 s	55.1 GB	10.11 s	19.2 GB
PF-LHM-L	1000 MB	160 K	11.20 s	55.8 GB	10.64 s	20.0 GB

4.2. Qualitative Results

As demonstrated in Fig. 8, we present the animation results of avatars generated from various in-the-wild monocular videos, including NeuMan [15], REC-MV [30], Vid2Avatar [7], MVHumanNet [49] and our causal video dataset. Our PF-LHM is capable of generalizing across different identities and garment styles, producing highly realistic renderings for novel human poses and arbitrary view-points.

4.3. Ablation Study

Model Efficiency Table 5 presents quantitative results that substantiate the efficiency of our model, tested on NVIDIA A100-80G hardware. The table clearly illustrates that our novel framework significantly outperforms the original LHM architecture, achieving notably reduced training times and lower memory consumption. Furthermore, during testing, our inference times are about 5~10 times faster than those of LHM.

Model Parameter Scalability To verify the scalability of our PF-LHM, we train variant models with increasing parameter numbers by scaling the layer numbers. Table 6 compares performance across various model capacities. Our experiments indicate that increasing the number

Table 6. Analysis of model parameters and 3D geometric point numbers.

Methods	# Points	PSNR \uparrow	SSIM \uparrow	LPIPS \downarrow	Time \downarrow	Memory \downarrow
PF-LHM-M	40 K	28.001	0.969	0.017	7.32 seconds	17 GB
PF-LHM-M	160 K	28.565	0.975	0.014	10.64 seconds	20 GB
PF-LHM-S	80 K	28.089	0.970	0.017	7.35 seconds	17 GB
PF-LHM-M	80 K	28.563	0.975	0.015	9.03 seconds	18 GB
PF-LHM-L	80 K	28.924	0.977	0.014	10.11 seconds	19 GB

of model parameters correlates with improved performance. Figure 5 presents the comparison among PF-LHM-S, PF-LHM-M, and PF-LHM-L where the larger model achieves more accurate reconstruction. Also, Fig. 6 depicts the performance of different models based on varying input view counts, clearly indicating that our model is scalable and that performance improves with an increased number of input images.

Number of Query Points Table 6 shows an ablation study analyzing the effect of varying the number of query points on public video datasets. As the number of query points increases from 40K to 80K, our model demonstrates improvements in PSNR, SSIM, and LPIPS by 0.562, 0.006, and 0.002, respectively. However, when the number of query points is increased further from 80K to 160K, we observe a slight gain in performance. Therefore, we set the number of query points to 80K to achieve an optimal balance between efficiency and model performance.

5. Conclusion

We present PF-LHM, a novel feed-forward framework for rapid and high-fidelity 3D human avatar reconstruction from one or a few casually captured, pose-free images. Our approach introduces the Encoder-Decoder Point-Image Transformer (PIT), which enables efficient multimodal fusion between geometric point tokens and sparse multi-view image tokens through hierarchical attention. By leveraging the PIT architecture, our method achieves superior scalability, generalization, and reconstruction quality while significantly reducing runtime compared to optimization-based baselines. Extensive experiments across synthetic and real-



Figure 4. Animatable human reconstruction comparisons from sparse images on in-the-wild videos.



Figure 5. Ablation study on model design and parameters.

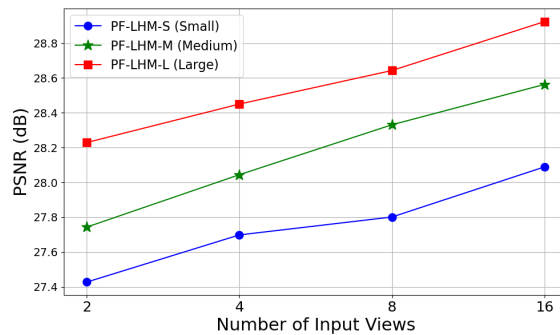


Figure 6. PSNR performance of our models with different input views.

world datasets demonstrate that PF-LHM effectively unifies single- and sparse-view reconstruction and supports realis-

tic avatar animation using 3D Gaussian Splatting.

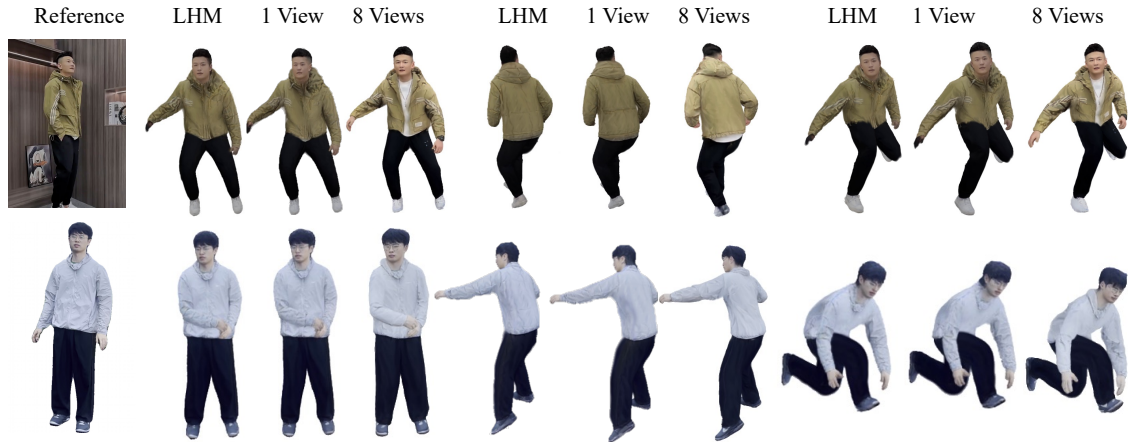


Figure 7. Comparison results of animatable human reconstruction methods with LHM.



Figure 8. Visual animation results of avatars created from monocular in-the-wild videos. The created 3D avatars can be animated using novel human poses and demonstrate highly detailed appearance. Also, the figure effectively illustrates the generalization capability of our approach, delivering outstanding results across various demographics, including the elderly, children, men, and women, as well as individuals of differing heights and body types.

References

- [1] Thiemo Alldieck, Marcus Magnor, Weipeng Xu, Christian Theobalt, and Gerard Pons-Moll. Detailed human avatars from monocular video. In *3DV*, 2018. 2
- [2] Thiemo Alldieck, Marcus Magnor, Weipeng Xu, Christian Theobalt, and Gerard Pons-Moll. Video based reconstruction of 3d people models. In *ICCV*, 2018. 2
- [3] Thiemo Alldieck, Gerard Pons-Moll, Christian Theobalt, and Marcus Magnor. Tex2shape: Detailed full human body geometry from a single image. In *ICCV*, 2019. 2
- [4] Yukang Cao, Guanying Chen, Kai Han, Wenqi Yang, and Kwan-Yee K Wong. Jiff: Jointly-aligned implicit face function for high quality single view clothed human reconstruction. In *CVPR*, 2022. 2
- [5] Vasileios Choutas, Lea Müller, Chun-Hao P Huang, Siyu Tang, Dimitrios Tzionas, and Michael J Black. Accurate 3d body shape regression using metric and semantic attributes. In *CVPR*, 2022. 2
- [6] Patrick Esser, Sumith Kulal, Andreas Blattmann, Rahim Entezari, Jonas Müller, Harry Saini, Yam Levi, Dominik Lorenz, Axel Sauer, Frederic Boesel, et al. Scaling rectified flow transformers for high-resolution image synthesis. In *ICML*, 2024. 2, 5
- [7] Chen Guo, Tianjian Jiang, Xu Chen, Jie Song, and Otmar Hilliges. Vid2avatar: 3d avatar reconstruction from videos in the wild via self-supervised scene decomposition. In *CVPR*, 2023. 3, 7, 8, 14
- [8] Chen Guo, Junxuan Li, Yash Kant, Yaser Sheikh, Shunsuke Saito, and Chen Cao. Vid2avatar-pro: Authentic avatar from videos in the wild via universal prior. In *CVPR*, 2025. 2, 3
- [9] Sang-Hun Han, Min-Gyu Park, Ju Hong Yoon, Ju-Mi Kang, Young-Jae Park, and Hae-Gon Jeon. High-fidelity 3d human digitization from single 2k resolution images. In *CVPR*, 2023. 6
- [10] Yicong Hong, Kai Zhang, Jiuxiang Gu, Sai Bi, Yang Zhou, Difan Liu, Feng Liu, Kalyan Sunkavalli, Trung Bui, and Hao Tan. Lrm: Large reconstruction model for single image to 3d. *arXiv preprint arXiv:2311.04400*, 2023. 3
- [11] Liangxiao Hu, Hongwen Zhang, Yuxiang Zhang, Boyao Zhou, Boning Liu, Shengping Zhang, and Liqiang Nie. Gaussianavatar: Towards realistic human avatar modeling from a single video via animatable 3d gaussians. In *CVPR*, 2024. 3, 7
- [12] Shoukang Hu and Ziwei Liu. Gauhuman: Articulated gaussian splatting from monocular human videos. In *CVPR*, 2024. 3
- [13] Boyi Jiang, Yang Hong, Hujun Bao, and Juyong Zhang. Selfrecon: Self reconstruction your digital avatar from monocular video. In *CVPR*, 2022. 3
- [14] Tianjian Jiang, Xu Chen, Jie Song, and Otmar Hilliges. Instantavatar: Learning avatars from monocular video in 60 seconds. In *CVPR*, 2023. 3, 7
- [15] Wei Jiang, Kwang Moo Yi, Golnoosh Samei, Oncel Tuzel, and Anurag Ranjan. Neuman: Neural human radiance field from a single video. In *ECCV*, 2022. 3, 7, 8, 14
- [16] Angjoo Kanazawa, Michael J Black, David W Jacobs, and Jitendra Malik. End-to-end recovery of human shape and pose. In *CVPR*, 2018. 2
- [17] Bernhard Kerbl, Georgios Kopanas, Thomas Leimkühler, and George Drettakis. 3d gaussian splatting for real-time radiance field rendering. *TOG*, 2023. 2, 4
- [18] Mengfei Li, Xiaoxiao Long, Yixun Liang, Weiyu Li, Yuan Liu, Peng Li, Xiaowei Chi, Xingqun Qi, Wei Xue, Wenhan Luo, et al. M-lrm: Multi-view large reconstruction model. *arXiv preprint arXiv:2406.07648*, 2024. 3
- [19] Peng Li, Wangguandong Zheng, Yuan Liu, Tao Yu, Yangguang Li, Xingqun Qi, Mengfei Li, Xiaowei Chi, Siyu Xia, Wei Xue, et al. Pshuman: Photorealistic single-view human reconstruction using cross-scale diffusion. In *CVPR*, 2025. 3
- [20] Siyou Lin, Hongwen Zhang, Zerong Zheng, Ruizhi Shao, and Yebin Liu. Learning implicit templates for point-based clothed human modeling. In *ECCV*, 2022. 6
- [21] Matthew Loper, Naureen Mahmood, Javier Romero, Gerard Pons-Moll, and Michael J Black. Smpl: a skinned multi-person linear model. *TOG*, 2015. 2
- [22] Jiahao Lu, Tianyu Huang, Peng Li, Zhiyang Dou, Cheng Lin, Zhiming Cui, Zhen Dong, Sai-Kit Yeung, Wenping Wang, and Yuan Liu. Align3r: Aligned monocular depth estimation for dynamic videos. *arXiv preprint arXiv:2412.03079*, 2024. 3
- [23] Gyeongsik Moon, Takaaki Shiratori, and Shunsuke Saito. Expressive whole-body 3d gaussian avatar. In *ECCV*, 2024. 3, 7
- [24] Maxime Oquab, Timothée Darcet, Théo Moutakanni, Huy Vo, Marc Szafraniec, Vasil Khalidov, Pierre Fernandez, Daniel Haziza, Francisco Massa, Alaaeldin El-Nouby, et al. Dinov2: Learning robust visual features without supervision. *arXiv preprint arXiv:2304.07193*, 2023. 5
- [25] Keunhong Park, Utkarsh Sinha, Peter Hedman, Jonathan T Barron, Sofien Bouaziz, Dan B Goldman, Ricardo Martin-Brualla, and Steven M Seitz. Hypernerf: A higher-dimensional representation for topologically varying neural radiance fields. *arXiv preprint arXiv:2106.13228*, 2021. 3
- [26] Georgios Pavlakos, Vasileios Choutas, Nima Ghorbani, Timo Bolkart, Ahmed AA Osman, Dimitrios Tzionas, and Michael J Black. Expressive body capture: 3d hands, face, and body from a single image. In *CVPR*, 2019. 2
- [27] Ben Poole, Ajay Jain, Jonathan T Barron, and Ben Mildenhall. Dreamfusion: Text-to-3d using 2d diffusion. In *ICLR*, 2023. 3
- [28] Zhiyin Qian, Shaofei Wang, Marko Mihajlovic, Andreas Geiger, and Siyu Tang. 3dgs-avatar: Animatable avatars via deformable 3d gaussian splatting. In *CVPR*, 2024. 3
- [29] Zhiyin Qian, Shaofei Wang, Marko Mihajlovic, Andreas Geiger, and Siyu Tang. 3dgs-avatar: Animatable avatars via deformable 3d gaussian splatting. In *CVPR*, 2024. 3
- [30] Lingteng Qiu and Guanying Chen. Rec-mv: Reconstructing 3d dynamic cloth from monocular videos. In *CVPR*, 2023. 3, 6, 7, 8, 14
- [31] Lingteng Qiu, Xiaodong Gu, Peihao Li, Qi Zuo, Weichao Shen, Junfei Zhang, Kejie Qiu, Weihao Yuan, Guanying

- Chen, Zilong Dong, and Liefeng Bo. Lhm: Large animatable human reconstruction model from a single image in seconds. In *arXiv preprint arXiv:2503.10625*, 2025. 2, 3, 4, 6, 7, 8
- [32] Lingteng Qiu, Shenhao Zhu, Qi Zuo, Xiaodong Gu, Yuan Dong, Junfei Zhang, Chao Xu, Zhe Li, Weihao Yuan, Liefeng Bo, et al. Anigs: Animatable gaussian avatar from a single image with inconsistent gaussian reconstruction. In *CVPR*, 2025. 3, 7
- [33] Shunsuke Saito, Zeng Huang, Ryota Natsume, Shigeo Morishima, Angjoo Kanazawa, and Hao Li. Pifu: Pixel-aligned implicit function for high-resolution clothed human digitization. In *ICCV*, 2019. 2
- [34] Shunsuke Saito, Tomas Simon, Jason Saragih, and Hanbyul Joo. Pifuhd: Multi-level pixel-aligned implicit function for high-resolution 3d human digitization. In *CVPR*, 2020. 2
- [35] Ruizhi Shao, Youxin Pang, Zerong Zheng, Jingxiang Sun, and Yebin Liu. Human4dit: 360-degree human video generation with 4d diffusion transformer. *TOG*, 2024. 6
- [36] Jeff Tan, Donglai Xiang, Shubham Tulsiani, Deva Ramanan, and Gengshan Yang. Dressrecon: Freeform 4d human reconstruction from monocular video. In *3DV*, 2025. 3
- [37] Jiaxiang Tang, Zhaoxi Chen, Xiaokang Chen, Tengfei Wang, Gang Zeng, and Ziwei Liu. Lgm: Large multi-view gaussian model for high-resolution 3d content creation. In *ECCV*, 2024. 3
- [38] Zhenggang Tang, Yuchen Fan, Dilin Wang, Hongyu Xu, Rakesh Ranjan, Alexander Schwing, and Zhicheng Yan. Mv-dust3r+: Single-stage scene reconstruction from sparse views in 2 seconds. *arXiv preprint arXiv:2412.06974*, 2024. 3
- [39] Boyuan Wang, Runqi Ouyang, Xiaofeng Wang, Zheng Zhu, Guosheng Zhao, Chaojun Ni, Guan Huang, Lihong Liu, and Xingang Wang. Humandreamer-x: Photorealistic single-image human avatars reconstruction via gaussian restoration. *arXiv preprint arXiv:2504.03536*, 2025. 3
- [40] Jianyuan Wang, Minghao Chen, Nikita Karaev, Andrea Vedaldi, Christian Rupprecht, and David Novotny. Vgg: Visual geometry grounded transformer. In *CVPR*, 2025. 3
- [41] Peng Wang, Hao Tan, Sai Bi, Yinghao Xu, Fujun Luan, Kalyan Sunkavalli, Wenping Wang, Zexiang Xu, and Kai Zhang. Pf-lrm: Pose-free large reconstruction model for joint pose and shape prediction. *arXiv preprint arXiv:2311.12024*, 2023. 3
- [42] Shuzhe Wang, Vincent Leroy, Yohann Cabon, Boris Chidlovskii, and Jerome Revaud. Dust3r: Geometric 3d vision made easy. In *CVPR*, 2024. 3
- [43] Zhou Wang, Eero P Simoncelli, and Alan C Bovik. Multiscale structural similarity for image quality assessment. In *The Thirty-Seventh Asilomar Conference on Signals, Systems & Computers*, 2003, 2003. 6
- [44] Zilong Wang, Zhiyang Dou, Yuan Liu, Cheng Lin, Xiao Dong, Yunhui Guo, Chenxu Zhang, Xin Li, Wenping Wang, and Xiaohu Guo. Wonderhuman: Hallucinating unseen parts in dynamic 3d human reconstruction. *arXiv preprint arXiv:2502.01045*, 2025. 3
- [45] Chung-Yi Weng, Brian Curless, Pratul P Srinivasan, Jonathan T Barron, and Ira Kemelmacher-Shlizerman. Humanerf: Free-viewpoint rendering of moving people from monocular video. In *CVPR*, 2022. 2, 3
- [46] Zhenzhen Weng, Jingyuan Liu, Hao Tan, Zhan Xu, Yang Zhou, Serena Yeung-Levy, and Jimei Yang. Template-free single-view 3d human digitalization with diffusion-guided lrm. *arXiv preprint arXiv:2401.12175*, 2024. 3
- [47] Xiaoyang Wu, Yixing Lao, Li Jiang, Xihui Liu, and Hengshuang Zhao. Point transformer v2: Grouped vector attention and partition-based pooling. In *NeurIPS*, 2022. 2, 4
- [48] Xiaoyang Wu, Zhuotao Tian, Xin Wen, Bohao Peng, Xihui Liu, Kaicheng Yu, and Hengshuang Zhao. Towards large-scale 3d representation learning with multi-dataset point prompt training. In *CVPR*, 2024. 5, 14
- [49] Zhangyang Xiong, Chenghong Li, Kenkun Liu, Hongjie Liao, Jianqiao Hu, Junyi Zhu, Shuliang Ning, Lingteng Qiu, Chongjie Wang, Shijie Wang, et al. Mvhumannet: A large-scale dataset of multi-view daily dressing human captures. In *CVPR*, 2024. 2, 8, 14
- [50] Yuliang Xiu, Jinlong Yang, Xu Cao, Dimitrios Tzionas, and Michael J Black. Econ: Explicit clothed humans optimized via normal integration. In *CVPR*, 2023. 2
- [51] Yuliang Xiu, Yufei Ye, Zhen Liu, Dimitrios Tzionas, and Michael J Black. Puzzleavatar: Assembling 3d avatars from personal albums. *TOG*, 2024. 3
- [52] Jianing Yang, Alexander Sax, Kevin J Liang, Mikael Henaff, Hao Tang, Ang Cao, Joyce Chai, Franziska Meier, and Matt Feiszli. Fast3r: Towards 3d reconstruction of 1000+ images in one forward pass. *arXiv preprint arXiv:2501.13928*, 2025. 3
- [53] Xihe Yang, Xingyu Chen, Daiheng Gao, Shaohui Wang, Xiaoguang Han, and Baoyuan Wang. Have-fun: Human avatar reconstruction from few-shot unconstrained images. In *CVPR*, 2024. 2
- [54] Xihe Yang, Xingyu Chen, Daiheng Gao, Shaohui Wang, Xiaoguang Han, and Baoyuan Wang. Have-fun: Human avatar reconstruction from few-shot unconstrained images. In *CVPR*, 2024. 3
- [55] Zhengming Yu, Wei Cheng, Xian Liu, Wayne Wu, and Kwan-Yee Lin. Monohuman: Animatable human neural field from monocular video. In *CVPR*, 2023. 3
- [56] Richard Zhang, Phillip Isola, Alexei A Efros, Eli Shechtman, and Oliver Wang. The unreasonable effectiveness of deep features as a perceptual metric. In *CVPR*, 2018. 6
- [57] Zechuan Zhang, Zongxin Yang, and Yi Yang. Sifu: Side-view conditioned implicit function for real-world usable clothed human reconstruction. In *CVPR*, 2024. 2
- [58] Shunyuan Zheng, Boyao Zhou, Ruizhi Shao, Boning Liu, Shengping Zhang, Liqiang Nie, and Yebin Liu. Gps-gaussian: Generalizable pixel-wise 3d gaussian splatting for real-time human novel view synthesis. In *CVPR*, 2024. 3
- [59] Zerong Zheng, Tao Yu, Yebin Liu, and Qionghai Dai. Pamir: Parametric model-conditioned implicit representation for image-based human reconstruction. *TPAMI*, 2021. 2
- [60] Yiyu Zhuang, Jiayi Lv, Hao Wen, Qing Shuai, Ailing Zeng, Hao Zhu, Shifeng Chen, Yujiu Yang, Xun Cao, and Wei Liu. Idol: Instant photorealistic 3d human creation from a single image. In *CVPR*, 2025. 2, 3, 7

- [61] Anton Zubekhin, Heming Zhu, Paulo Gotardo, Thabo Beeler, Marc Habermann, and Christian Theobalt. Giga: Generalizable sparse image-driven gaussian avatars. *arXiv preprint arXiv:2504.07144*, 2025. [3](#)

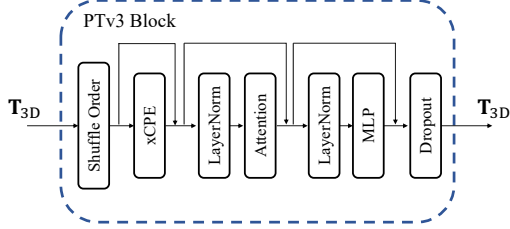


Figure 9. Detailed architecture of PTv3 Block [48].

Table 7. **Ablation study on dataset scalability.** The metrics are calculated based on 16-view image inputs.

Methods	PSNR \uparrow	SSIM \uparrow	LPIPS \downarrow
PF-LHM-L + Synthetic Data	26.148	0.952	0.027
PF-LHM-L + 10K Videos	27.456	0.970	0.018
PF-LHM-L + 100K Videos	28.312	0.975	0.017
PF-LHM-L + All	28.924	0.977	0.014

A. Implementation Details

A.1. Details of Points Serialization

To trade the scalability and efficiency of our feed-forward framework, we leverage serialization to transform unstructured SMPL-X anchor points into structured data format. Following Point Transformer v3 (PTv3) [48], we mixture 4 patterns of serialization, including Z-order, Hibert, Trans Z-order and Trans Hibert, and apply random shuffle to the order of serialization patterns before each PTv3 block.

A.2. Details of PTv3 Block

As illustrated in Fig. 9, our point attention architecture integrates the mechanism introduced in Point Transformer v3 [48]. This architecture employs patch-based self-attention to accelerate the forward pass. Furthermore, Grip Pooling is utilized to downsample the point cloud, enhancing the efficiency of point cloud self-attention. Importantly, to facilitate interaction among different patch groups, a shuffling order is implemented.

In our setup, the patch sizes are set to 4096, 2048, and 1024 for the 80K point clouds, decreasing in accordance with the downsampling process. For the 160K point clouds, the patch sizes are configured to 8192, 4096, and 2048.

B. Experiments

B.1. Details of Testing Dataset

For our qualitative results, we utilize videos from Vid2Avatar [7], specifically those indexed as: *00000_random*, *00020_Dance*, *00069_Dance*, *exstri-malik*, and *Yuliang*. Additionally, we draw on videos from Rec-MV [30], including the following indices: *anran_dance_self_rotated*, *anran_purple*, *anran_skirt*, *self-rotate-leyang*, and *xiaolin*. Moreover, we use the

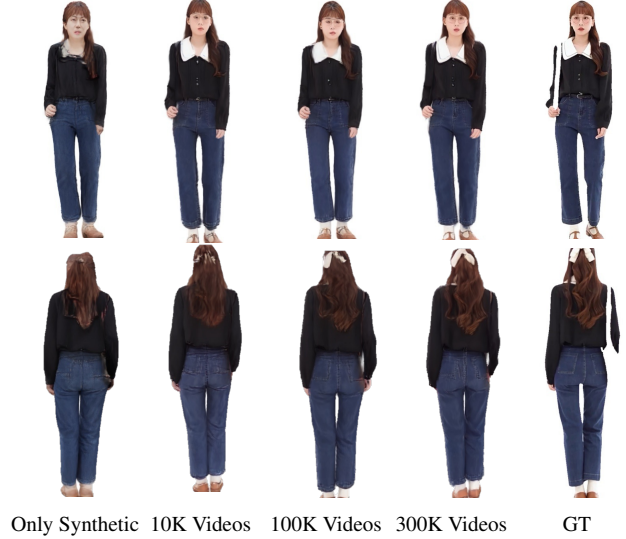


Figure 10. Ablation study on dataset scalability.

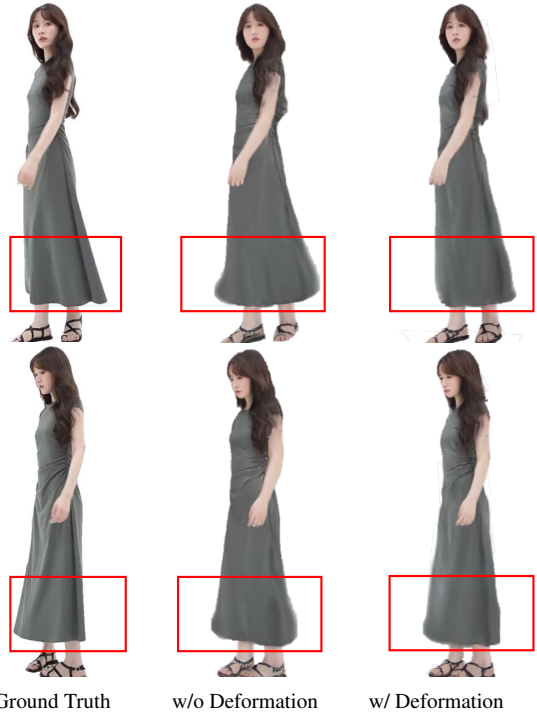


Figure 11. The ablation study for posed-conditioned deformation. The red boxes highlight the visual difference mentioned above.

NeuMan [15] dataset with the indices: *citron* and *seattle*. And, sparse view images are randomly sampled from MVHumanNet [49], with the following indices: 101330, 101425, 101483, 103383, 103528, 104013, 203243, and 103594, along with videos captured using our smartphone.

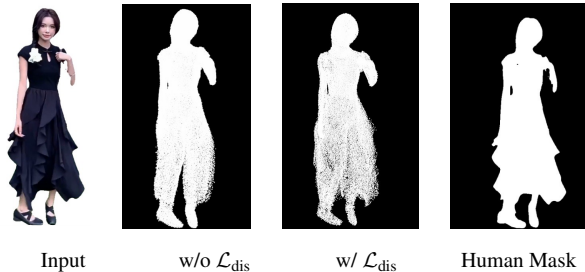


Figure 12. The ablation study for mask distribution loss.

B.2. More Ablation Study

Details of Dataset Scalability To assess the scalability of our dataset, we perform controlled experiments utilizing stratified random subsets of 10K and 100K from the original training dataset of 300K videos. Table 7 demonstrates that relying solely on the synthetic dataset leads to poor model generalization. In contrast, incorporating an in-the-wild dataset significantly improves the model’s robustness and performance during real-world evaluations. Furthermore, increasing the size of the dataset significantly improves model results, although the gains in performance tend to diminish with larger dataset sizes. Figure 10 illustrates the findings of our ablation study regarding dataset scalability.

Mask Distribution Loss Gaussian models tend to learn large-scale Gaussian primitives rather than large step offsets. To address this issue, we introduce a mask distribution regularization loss that encourages Gaussian primitives to learn offsets instead of concentrating on large-scale axes. As illustrated in Fig. 12, employing this loss enables the mean position of the Gaussian primitives to be distributed more evenly across the ground truth mask area, thereby preventing the model from learning large-scale axes of the Gaussian primitives.

Posed-Condition Deformation Figure 11 illustrates the impact of using pose-conditioned deformation. The results clearly indicate that our deformation tokens, which are conditioned on SMPL-X parameters, effectively model non-rigid deformations of loose garments, in contrast to the case without pose conditioning.

B.3. More Results

Figure 13 presents more animation results using eight input images. Our method enables high-fidelity reconstruction and animation of human avatars through the efficient Point-Image Transformer architecture, thereby demonstrating robust generalization capabilities and practical effectiveness.

C. Limitations and Future Work

A primary limitation of our approach lies in its reliance on the SMPL-X template mesh for initializing geometric tokens. While this offers a strong structural prior, it can constrain reconstruction fidelity for subjects wearing loose or non-body-conforming garments, such as dresses, which deviate significantly from the SMPL-X topology. Additionally, due to the limited diversity of large motion poses in our training datasets, the model’s performance may degrade when encountering unseen or extreme poses. In future work, we plan to investigate more flexible garment representations and explore pose-independent anchor structures to better capture complex clothing dynamics and improve generalization to diverse motions.



Reference

Animation Results

Figure 13. More animation results of avatars created with 8-image inputs. **Reference** image is one of the input images.